

# Simultaneous measurement of Raman and nonlinear optical tensors

Volodymyr Multian,<sup>†,‡,¶</sup> Luigi Bonacina,<sup>‡</sup> and Jérémie Teyssier<sup>\*,†</sup>

<sup>†</sup>*Department of Quantum Matter Physics, University of Geneva, 24 Quai Ernest Ansermet, Geneva CH-1211, Switzerland*

<sup>‡</sup>*Nonlinear BioImaging Lab, Department of Applied Physics, University of Geneva 24 Quai Ernest Ansermet, Geneva CH-1211, Switzerland*

<sup>¶</sup>*Photon Processes Department, Institute of Physics of NAS of Ukraine. Prospect Nauky, 46, Kyiv-03028, Ukraine.*

E-mail: jeremie.teyssier@unige.ch

## Abstract

Raman spectroscopy and Second Harmonic Generation (SHG) are complementary, non-destructive techniques that provide rich and distinct insights into the structural and electronic properties of materials. Raman spectroscopy offers detailed information on vibrational modes, phase transitions, temperature, and local stress, while SHG is highly sensitive to symmetry and orientation, particularly in non-centrosymmetric structures. In this work, in addition to combining both techniques, we propose a novel approach to determine the nonlinear optical tensor, leveraging the spatial and ultra-fast temporal offset of a Bessel-Gaussian laser beam at the microscope's focal point.

## Keywords

Raman, SHG, MRANHG

# 1 Introduction

Raman spectroscopy and Second Harmonic Generation (SHG) are powerful, complementary techniques that offer unique insights into the properties of materials. Each method provides distinct information, which, when combined, allows for a comprehensive understanding of a material's structural and electronic characteristics.

**Raman Spectroscopy** provides detailed information about the vibrational modes of molecules and crystals, as well as electronic and magnetic susceptibilities. It is highly sensitive to changes in chemical composition, in structural, electronic, or magnetic phase transitions, and to stress/strain within a material.

**Second Harmonic Generation (SHG)**, on the other hand, is a nonlinear optical process particularly sensitive to the symmetry properties at the microscopic level. SHG is often used to probe structural properties at interfaces, detect structural changes, or image non-centrosymmetric arrangements.

Combining Raman and SHG techniques offers several compelling advantages. Both are non-destructive, making them especially valuable for monitoring processes without altering the sample. This synergy is particularly beneficial for obtaining a comprehensive view of complex materials.

Polarization-dependent measurements enhance the specificity and sensitivity of both techniques. In Raman spectroscopy, polarization analysis helps identify the symmetry of vibrational modes. In SHG, it is essential for determining the symmetry properties, like stacking in 2D materials or heterostructures, or crystal orientation. Pushed to their limit, polarimetric SHG and Raman collection allows to extract the full 2nd order susceptibility and Raman tensors, respectively.

The simultaneous measurement of polarization-dependent Raman and SHG signals is applicable across diverse fields, including materials science, biology, chemistry, and nanotechnology. For instance, in biological tissues, Raman spectroscopy can provide biochemical information, while SHG can image structural proteins like collagen and myosin.<sup>1</sup> This dual

capability enhances the ability to study complex biological structures and dynamic processes.

In this work, we introduce a new experimental setup that combines Raman and SHG microscopy. We will present the specificity of both Raman and SHG sub-systems and the technical challenges for coupling the two technics with preserving full polarization control for both excitation lasers and collected signals. A completely new approach is proposed to reliably and rapidly extract the nonlinear and Raman optical tensors. We will detail the experimental aspects of this implementation as well as data analysis, which relies on a polarization-resolved ray-tracing model for data fitting.

## 2 Experimental setup

The optical system we developed for simultaneous polarization-resolved micro-Raman and Microscopic Rotational Anisotropy Second Harmonic Generation (MRA-SHG) is illustrated in Figure 1, a complete scheme of the instrument is provided in the supporting information (SI). The optical integration between the commercial confocal Raman microscope (Section 2.1) and the SHG subsystem (Section 2.2) relies on a polarization maintaining dichroic beam splitter module we specially developed for this purpose<sup>2</sup> (Section 2.3).

### 2.1 Raman subsystem

We use a commercial Raman microscope (Horiba LabRAM HR Evolution) equipped with several lasers emitting from 405 nm to 647 nm in confocal configuration with a spectral resolution of  $0.3 \text{ cm}^{-1}$  (0.04 meV). A fine and continuous control of the power in a range from  $1 \mu\text{W}$  to  $40 \text{ mW}$  (power control unit PCU2) is achieved using a half-wave plate (ThorLabs AHWP05M-600) mounted on a motorized rotation stage, a Glan-Laser polarizer (ThorLabs GL10, extinction ratio 100 000:1) combined with the built-in neutral density filter set. For controlling polarization, we developed a polarization state generator (PSG) based on quarter-wave (ThorLabs AQWP05M-600) and half-wave (ThorLabs AHWP05M-600) plates

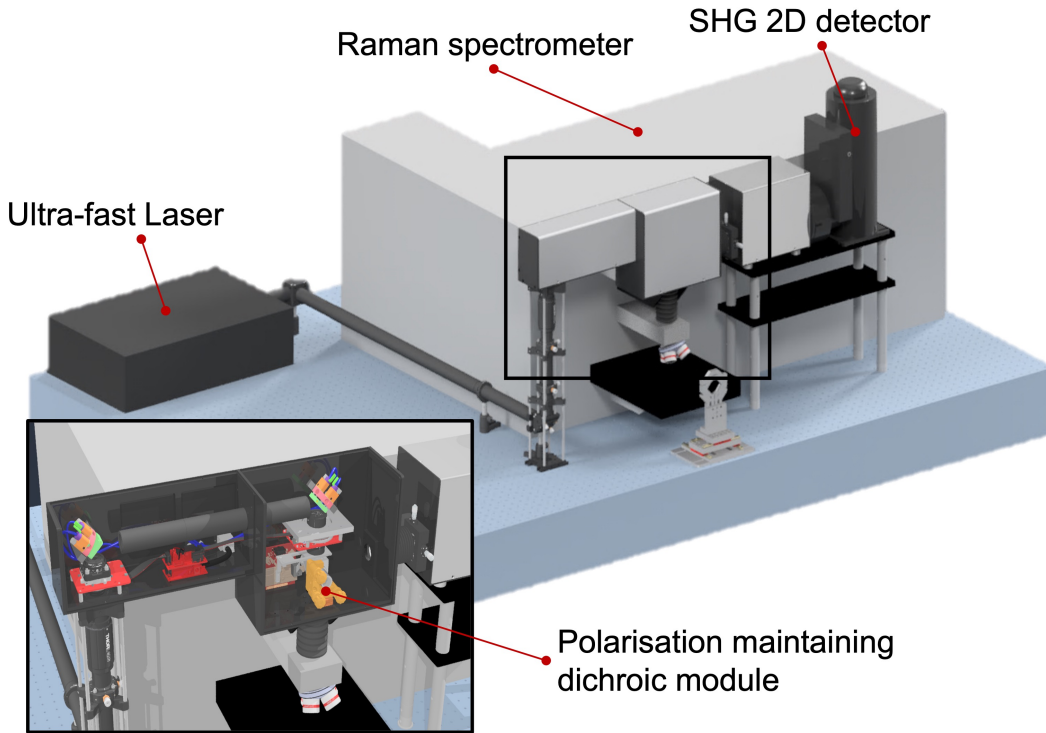


Figure 1: overview of the experimental setup for simultaneous Raman and SHG measurements with a close-up on the lasers coupling region. A detailed Scheme is provided in Figure SM-1

on motorized stages, providing continuous tuning of the polarization from circular-left, linear, to circular-right. Synchronized with the power control unit, PSG allows to pre-compensate for polarization distortions on the optical path as described by several authors.<sup>3-6</sup> Analysis of the polarization state of the Raman signal was achieved by placing a Glan-Laser polarizer (ThorLabs GL10) mounted in the motorized rotation stage at the entrance of the spectrometer. Signal acquisition was performed with LN cooled Si charge-coupled device (CCD) array (Horiba Scientific Symphony II).

Temperature dependencies of Raman and SHG signals are measured in a flow cryostat (Konti Micro from CryoVac GMBH) in a temperature range from 4K to 350K and by using a laser to locally heat the sample for temperatures above ambient conditions. We recently

used Raman spectroscopy to locally control the temperature of samples by tuning the power of the laser and monitoring the temperature via the Stokes and anti-Stokes ratio.<sup>7</sup> The present setup allows Raman spectroscopy to be used as a furnace and a thermometer, and recent software developments have made the extraction of temperature, including black body radiation corrections, straightforward.<sup>8</sup>

## 2.2 SHG subsystem

For SHG measurements, we coupled a Ti:Sapphire oscillator (Coherent Vitesse 800 nm, 100 fs, 80 MHz) with a custom-made module (close-up panel in Figure 1) featuring a power control unit, two piezo actuated mirrors for beam steering, half-wave plate on motorized rotation stage, and non-polarizing dichroic module for coupling pulsed and CW lasers and splitting pump and SHG (see details in Section 2.3). A set of two axicons (ThorLabs AX122, 2.0°, Uncoated UVFS) is used to shape the fs laser beam from Gaussian to a Bessel-Gaussian (BG) distribution with a diameter of  $\sim$ 4.5 mm and focus it onto the same spot as the Raman CW laser with size 1.0  $\mu$ m (FWHM) through a refractive-window-corrected 63 $\times$  objective.

SHG signal at 400 nm is collected in epi-detection geometry in a separate optical channel using a LN-cooled CCD array (Princeton Instruments). A cascade of 3 band-pass interference filters was used for blocking the pump beam (ThorLabs FBH400-10, CWL = 400 nm, FWHM = 10 nm). The signal can be acquired in parallel and crossed configurations with respect to the incidence polarization with the use of a Glan-Thompson polarizer (ThorLabs GTH10M) mounted in a motorized stage in front of the CCD. The fs laser heating is estimated by Raman-based thermometry performed on the same spot.

## 2.3 Non-polarizing beam splitter

Each optical element on the optical path that refracts or reflects the beam distorts the polarization. Significant polarization distortion arises when optical elements such as reflective mirrors, beam splitters, and dichroic mirrors are used far from normal incidence. This

problem can be solved by an approach based on compensation of polarization distortion from an optical element by adding an identical rotated optical element to compensate polarization distortion in  $P$  and  $S$  channels as described in the works of Cox and Bélanger.<sup>9,10</sup> In previous work, we consolidated these concepts in a single integrated module that can operate as a non-polarizing dichroic mirror in transmission and reflection geometry.<sup>2,11</sup>

### 3 Nonlinear optical tensor extraction

#### 3.1 Experimental approach

In the electrical dipole approximation, the nonlinear polarization  $\vec{P}$ , involved in SHG process, can be written as:<sup>12</sup>

$$P_i = \epsilon_0 \chi_{ijk}^{(2)} E_i E_j, \quad (1)$$

where  $E_{i,j}$  refers to the electrical field of pump beam and  $\chi_{ijk}^{(2)}$ , the tensor of second order nonlinear susceptibility. Here and further in the text, we use Einstein's summation formalism, which assumes the summation of over repeated indices. Equation 1 describes the efficiency of the emitted SHG in the 3D space of the laboratory frame. The tensor  $\chi_{ijk}^{(2)}$  is a rank 3 tensor ( $3 \times 3 \times 3$ ) which contains 27 complex elements. For a given compound, the structural point group defines identical and zero elements in the tensor. Higher symmetry implies a lower number of independent tensor elements.

Rotational Anisotropy Second Harmonic Generation (RA-SHG) is a well established experimental method to determine the quadratic nonlinear susceptibility tensor,  $\chi^{(2)}$ . Originally developed to study crystallographic and electronic symmetries in bulk materials, RA-SHG offers a rapid approach to characterize the SHG polarization dependence.<sup>13–15</sup> Specifically, a laser beam with either  $P$  (parallel) or  $S$  (perpendicular) polarization illuminates a sample at a fixed angle of incidence. SHG intensity is acquired while rotating the sam-

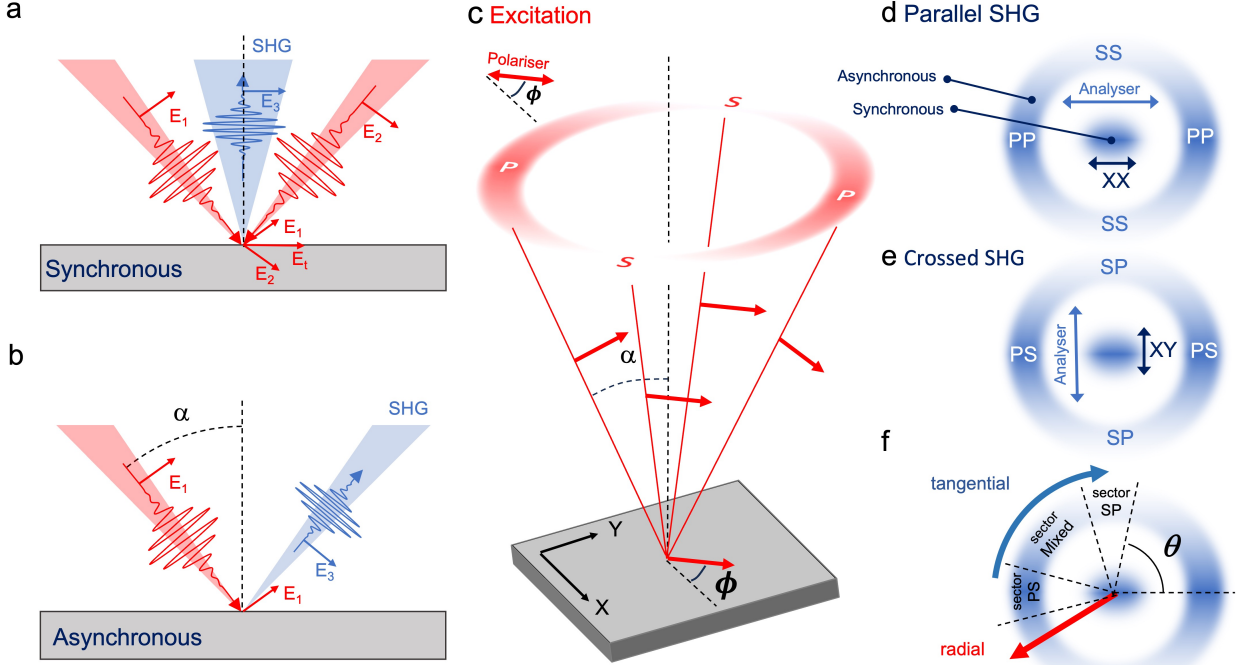


Figure 2: a) Polarization state at the focal point of BG beam excitation (in red) under a) synchronous and b) asynchronous conditions. c) Azimuthal dependence of the polarization state for the excitation BG beam polarized at an angle  $\phi$  relative to the sample x-axis. d-e) Corresponding patterns and polarization configurations for the (SHG) signal. The central part corresponds to the synchronous state probing normal incidence configuration XX, XY (S and P states are equivalent), while the ring is associated with the fixed incidence asynchronous polarization configuration. f) Definition of the different sectors and angles used for data analysis.

ple around the optical axis and varying the excitation/detection polarization settings ( $P/P$ ,  $P/S$ ,  $S/P$ ,  $S/S$ ). The polarization dependence of the resulting signal is fitted to a response calculated from the nonlinear susceptibility tensor and the specific experimental geometry. The accurate identification of the  $\chi^{(2)}$  tensor elements depends on knowledge of the crystal's symmetry (point group) and its orientation. Higher symmetry limits both the number of independent tensor components and the number of sample orientations required for a reliable fitting. Conversely, when the nonlinear tensor is known, it can be used to infer the crystal's orientation.

In a typical RA-SHG setup, the sample is excited by a linearly polarized ( $P$  or  $S$ ) pump beam at an angle  $\alpha$  to the surface normal, and the emitted SH signal is analyzed

with the polarizer along the  $S$  or  $P$  orientations. A complete analysis requires rotating the sample around its normal axis, producing four polarization-resolved curves based on the input/output configuration:  $P/P$ ,  $P/S$ ,  $S/P$ ,  $S/S$ . By fitting these curves, the  $\chi^{(2)}$  tensor can be reconstructed. This method is effective for parallel or weakly focused laser beams but is limited in spatial resolution or sample size. For micron-scale resolution, RA-SHG must be adapted to microscope geometries,<sup>1,16–19</sup> which poses challenges such as precise sample rotation at the microscale. A common solution is rotating the laser beam’s polarization using retardation optics.<sup>20</sup> Tight focusing required in high-resolution optical measurements involves objectives with high numerical aperture that introduce polarization distortions,<sup>21,22</sup> causing mismatches between the polarization states at focal point and at the back-focal aperture. Moreover, pulsed laser excitation, needs precise wavefront control. Ultrashort laser pulses passing through different glass thicknesses experience wavefront distortion, leading to variations in pulse arrival times at the focused beam waist, resulting in polarization distortions.<sup>23</sup> These distortions can cause misinterpretation of polarization dependencies when using a single sensor. Minimizing time delays with adaptive optics<sup>24</sup> and addressing refraction-induced polarization distortions with tailored opto-mechanical solutions<sup>25–27</sup> are necessary. Even when the polarization state and the spatial phase profile of the incoming light are pre-compensated, the approach is limited to the excitation path but cannot correct for light emitted by the sample.

In this work, we introduce a new Microscopic Rotational Anisotropy Second Harmonic Generation (MRA-SHG) method that overcomes many of these challenges by exploiting intrinsic wavefront distortions, imperfect spatial and temporal focusing in tightly focused beams, and self-phase-matching effects<sup>28–31</sup> to extract maximum information about 3D non-linear optical response of the material. We propose leveraging the inherent imperfections in spatial and temporal focusing found in real optical systems, rather than compensating for them. This is achieved by maximizing the information extracted from a single-point measurement through the use of an BG (annular or donut) beam, in place of the conventional

Gaussian laser beam profile.<sup>30-33</sup> The benefit of such configuration is detailed in Figure 2. When a sample is excited by a BG-shaped beam, it emits a complex pattern, which can be captured on a 2D imaging sensor placed in the Fourier plane of the objective. When photons from opposite sides of the optical axis coincide in time and space at the focal plane, interference occurs, resulting in an in-plane polarization component ( $\vec{E}_t = \vec{E}_1 + \vec{E}_2$  in Figure 2a) and the emission of a harmonic signal normal to the surface. This emission is detected as a sharp peak in the center of the Fourier pattern (spatiotemporal overlap spot in Figure 2d,e). This portion of the image enables to record the polar map at normal incidence. On the other hand, photons reaching the sample with unbalanced time-delay or having no spatial overlap with photons from opposite side of the optical axis, contribute to an out-of-plane excitation geometry (Figure 2b) and provide a measurement at a fixed angle of incidence ( $\alpha$  in Figure 2b-c). This emission, with no spatiotemporal overlap, is collected as a ring on the 2D detector as shown in Figure 2d,e. To our best knowledge, the simultaneous acquisition of SHG upon both in- and out-of-plane excitation at a given polarization angle  $\phi$  has never been exploited so far. This approach does not require any mechanical adjustment, reducing the measurement time ultimately to the integration time of the CCD camera. The normal incidence dataset is obtained by integrating the central region of the Fourier plane image for each polarization angle  $\phi$  (Figure 2d,e).

In addition to providing a comprehensive analysis of high-symmetry point groups in the *PS*, *SP*, *PS*, and *PP* maps, where only a limited number of tensor elements are involved, the use of ray tracing and evolutionary algorithms (see Section 3.2) allows the full information contained in the 2D pattern to be exploited, rather than relying on averaged signals from the *PS*, *SP*, *PS*, and *PP* sectors, as shown in Figure 2f. Indeed, the radial component contains the dependence of the signal to the angle of incidence  $\alpha$  (red arrow in Figure 2f) and the tangential component provides a continuous variation from one high symmetry point to another. It can be computed and fitted integrally (blue arrow in Figure 2f) capitalizing on the information contained in mixed polarization states. The approach to analyze this

complex 2D pattern is detailed in the following sections.

### 3.2 Data Analysis

The 2D image collected at Fourier plane reflects many interactions along the excitation and emission paths, involving both linear and nonlinear processes. Because a full analytical description would be impractically complex, we use a ray-tracing based model to simulate the influence of each optical element, with details provided in SI. This approach can be summarized to few key elements:

- introducing a grid of "polarized beamlet" instances characterized by positions in 3D space  $\vec{r}$ , complex beam parameters  $q$  defining the local curvatures of the wave front, polarization states described by electrical field in form of 3D Jones vectors  $\vec{E}^\omega$  defined in global coordinate system with corresponding wave vectors  $\hat{k}^\omega$ ;
- propagation  $\vec{r}$  and  $\hat{k}$  of "polarized beamlets" in 3D space according to ray tracing rules and transformation of electrical field  $\vec{E}^\omega$  at each interface with the use of  $P$ -matrix approach;
- calculation of effective vector field distribution  $\vec{E}^{\omega,\text{eff}}$  in the sample;
- calculation of response electrical field  $\vec{E}^{NLO}$  from effective field  $\vec{E}^{\omega,\text{eff}}$ ;
- rejection of electrical field of generated  $\vec{E}^{NLO}$  on the emission directions  $\hat{k}^{NLO}$ ;
- propagation of emitted "polarized beamlets" through the detection channel to the detector with the analyzer oriented in parallel or crossed configuration;
- calculation of the Fourier images by integration of resampled beamlets intensities at the detection plane.

The next step is to fit parameters describing the material's symmetry, orientation, and relevant optical properties in the ray-tracing model so that the simulated Fourier-plane

patterns match the experimental ones. (Figure 3a,b). Because the parameter space is high-dimensional and complex, we use a global optimization approach based on GPU-accelerated evolutionary algorithms. This allows us to fit multiple polarization configurations simultaneously and to incorporate datasets taken at different sample orientations keeping the material properties identical, improving the robustness and accuracy of the extracted parameters (SI, Section 2).

To simplify the visualization of both raw and fitted data without inspecting each individual Fourier image, we construct a single composite image that gathers all relevant information. The procedure to go from the Fourier plane raw and fitted data to this new polar maps is detailed in Figure 3c-e. For an incident light with a polarization angle  $\phi_n$ , we analyze each Fourier image and extract intensity by integration of region at fixed radius and azimuth angles  $\theta_m$  to form the map at the coordinates  $(\theta, \phi)$ . The integration of signal intensity of central part of the images in Fourier plane as a function of incident polarisation defines a polar plot that represents in-plane response (see Figure 3e) .

## 4 Experimental results

We first acquired Raman and SHG data from  $\text{KH}_2\text{PO}_4$  (KDP), a well-characterized nonlinear crystal with a known  $\chi^{(2)}$  tensor.<sup>34</sup> Its low-temperature phase transition was used to correlate the temperature dependence of the Raman response with that of second-harmonic generation. Polarimetric SHG measurements were then employed to calibrate the system, enabling quantitative extraction of the nonlinear tensor elements.

The approach was subsequently applied to  $\text{LiNbO}_3$ , to demonstrate the robustness of RA-SHG for determining absolute tensor element values.

## 4.1 Raman-SHG correlation

At room temperature,  $\text{KH}_2\text{PO}_4$  (KDP) is in a para-electric phase (P-KDP) with space group  $I\bar{4}2d$  ( $D_{2d}$ ) and ferroelectric phase (F-KDP) below  $T_c = 123$  K with space group  $Fdd2$  ( $C_{2v}$ ). KDP is known for high transmittance, high damage threshold, and is available in large single crystal dimensions, but it has low SHG efficiency due to relatively weak nonlinear coefficients at room temperature ( $d_{36} \approx 0.4$  pm/V @1064 nm<sup>34</sup>).

The KDP crystals used in this study were grown from saturated water solutions and annealed to remove internal moisture.<sup>35</sup> Figure 4 shows Raman (a) and total SHG (b) temperature-dependent signal recorded simultaneously from the same sample spot. Temperatures extracted from the Stokes/anti-Stokes fit of Raman spectra recorded when both excitation lasers are on, match those from the cryostat sensor, confirming negligible laser heating due to low crystal absorption. As temperature elevation due to light absorption in the material depends on many parameters like absorbance, thermal conductivity or thermal coupling with the substrate, using the Raman signal is a reliable way to directly estimate the focal point's temperature.

By cooling down below the phase transition temperature ( $T = 123$  K, dashed line in Figure 4a,b), SHG increases by two orders of magnitude as expected when ferroelectric polarization sets-in. Concomitantly, Raman spectra reveal a clear lowering of symmetry through an increase in the number of active Raman modes.

To the best of our knowledge, this is the first time that Raman spectroscopy has been conclusively used as a thermometer to verify the temperature of a distinct optical process.

## 4.2 Multiple entry calibration

MRA-SHG was performed at room temperature on prismatic sectors of the crystal of the tetragonal phase ( $\approx 3 \times 5 \times 2$  mm) of KDP for different orientations. They show a bright intensity "ring" and a faint central spot, which, although symmetry-forbidden for this material, can be attributed to slight misalignment in the normal-incidence setup.

The proposed data analysis allows to jointly analyze the responses from the studied material and a calibration sample, measured under identical conditions. In addition, different measurements such as SHG and Raman can be combined because they are acquired from the same sample position. This shared geometry constrains the sample orientation and significantly improves the robustness of tensor element determination for both SHG and Raman, even when the model involves a large number of parameters.

For the calibration of SHG and Raman response of the instrument we used KDP as reference. Additionally, we fix the known geometrical parameters of the experimental setup including distances between optical elements, parfocal and working distances of the objective, numerical aperture and entrance pupil diameter, precise retardance of the HWP, and extinction ratio of the attenuator. The remaining parameters, like tensor elements, Jones matrix elements of objectives, orientation of the crystals, etc., are globally fitted.

Figure 5 presents polarization maps and plots extracted from both raw and fitted SHG Fourier-plane patterns, along with polar plots of Raman intensity acquired from reference KDP and  $\text{LiNbO}_3$  crystals both with two distinct orientations.

Quality of the orientation determination can be concluded from the agreement of fitted crystal axes orientation with those on optical image presented in first row of Figure 5.

The datasets for a given material were fitted with a unique nonlinear optical tensor, transformed by a tensor rotation procedure (SI) to account for the different crystal orientations. Small misalignment of the surface orientation are taken into account by considering nonzero angle between the optical axis and the normal to the surface (SI). While each individual data input captures only a fraction of the complete response combining multiple inputs (such as different polarization states and orientations) enables a precise determination of tensor elements, including those that are typically inaccessible in conventional measurement geometries.

$\text{LiNbO}_3$  belongs to the  $C_{3v}$  point group with  $\chi^{(2)}$  tensor:

$$\chi^{(2)}(C_{3v}) = \left( \begin{array}{c} \left[ \begin{array}{ccc} 0 & xyx & yzy \\ xyx & 0 & 0 \\ yzy & 0 & 0 \end{array} \right], \\ \left[ \begin{array}{ccc} xyx & 0 & 0 \\ 0 & -xyx & yzy \\ 0 & yzy & 0 \end{array} \right], \\ \left[ \begin{array}{ccc} zyy & 0 & 0 \\ 0 & zyy & 0 \\ 0 & 0 & zzz \end{array} \right] \end{array} \right) \quad (2)$$

Assuming Kleinman symmetry, the number of free parameters in the tensor can be reduced to 3. In our case, this assumption holds because we excite the system with 1.55 eV (800 nm) photons, well below  $\text{LiNbO}_3$  indirect bandgap (3.3 eV), even when two-photon absorption is considered.<sup>36</sup> In this case, the  $(zyy)$  and  $(yzy)$  elements become identical.

Table 1 presents a comparison between tensor elements reported in the literature and those measured in the present study. Sign of elements are reported as published but only relative sign differences in the tensor are relevant.

Table 1: Comparison of reference data and estimated  $\chi^{(2)}$  tensor elements for  $\text{LiNbO}_3$  measured under  $fs$  laser excitation at 800 nm

$\chi^{(2)}$ element	Wavelength $\lambda$ , nm	Ref. value, pm/V	Ref.	This work, pm/V
$zzz$	852	51.4	<sup>37</sup>	
	1064	-54.0	<sup>38</sup>	$-51.5 \pm 2.0$
	1058	-83.4	<sup>39</sup>	
$zyy$	852	9.6	<sup>37</sup>	
	1064	-8.6	<sup>38</sup>	$-9.1 \pm 1.0$
	1058	-9.3	<sup>39</sup>	
$yzy$				$-9.6 \pm 1.0$
$xyx$	1064	-4.2	<sup>38</sup>	
	1058	-4.9	<sup>39</sup>	$-1.5 \pm 1.0$

Within the measurement uncertainty estimated from the fitting procedure, our results are in good agreement with previous reports. Moreover, the  $(zyy)$  and  $(yzy)$  elements exhibit identical values within the experimental error, confirming the validity of Kleinman symmetry.

In this model, SHG provides rich features that fix the crystal orientation, enabling reliable analysis of the more limited Raman response.

In theory,  $(A_1)$  mode of KDP under study is expected to be polarization independent, according to the selection rules for in-plane excitation of the investigated crystal orientations. It is defined by following Raman tensor:

$$R(A_1) = \begin{pmatrix} a & 0 & 0 \\ 0 & a & 0 \\ 0 & 0 & b \end{pmatrix}, \quad (3)$$

where  $a = 1$  and  $b = 0.8$  according to.<sup>40</sup>

Several studies have reported the presence of measurement artifacts in Raman responses,<sup>40,41</sup> consistent with our observations. While polarization in the SHG subsystem is well preserved by the non-polarizing module, the Raman response is strongly modulated by the spectrometer. The observed polarization-dependent signal, therefore, arises from a combination of the system response and out-of-plane leakage under tight focusing.

By constraining the crystal orientation through the SHG fitting, we calibrate the polarization response of the Raman setup and subsequently extract the Raman tensor of the  $(E)$  mode in  $\text{LiNbO}_3$ . According to the computational Raman database,<sup>42</sup> the  $(E)$  mode observed experimentally at  $580 \text{ cm}^{-1}$  corresponds to the calculated one at  $569 \text{ cm}^{-1}$ , which is characterized by the following Raman tensor:

$$R(E@569\text{cm}^{-1}) = \begin{pmatrix} -1.5 & 1.3 & -3.4 \\ 1.3 & 1.5 & 3.8 \\ -3.4 & 3.8 & 0.0 \end{pmatrix}, \quad (4)$$

We perform the fitting with an arbitrary symmetric Raman tensor with 6 free parameters:

$$R_{sym} = \begin{pmatrix} a & d & e \\ d & b & f \\ e & f & c \end{pmatrix} \quad (5)$$

A separate fitting exclusively applied to the Raman response with this number of free parameters and in presence of strong distortion of polarization by the optical system would not converge to a reliable set of values. Constraining Raman by the input from SHG by our comprehensive approach significantly improves the result.

Fitting gives us the following results normalized to match the  $a$  element of the calculated tensor:

$$R(E@580\text{cm}^{-1})_{fit} = \begin{pmatrix} -1.5 & 1.8 & -0.3 \\ 1.8 & 1.8 & 2.5 \\ -0.3 & 2.5 & -2.9 \end{pmatrix}. \quad (6)$$

Most of the fitted tensor elements are in good agreement with the calculated values. The largest discrepancies are observed for the  $c$  and  $e$  elements, which correspond to directions along the optical axis of the crystal. In addition, the fitting procedure correctly reproduces the sign of most tensor elements. The differences in the  $c$ ,  $e$ , and  $f$  elements may be attributed to variations in surface treatment among the investigated  $\text{LiNbO}_3$  crystal faces, which can lead to changes in Raman peak amplitudes, as reported in Ref. 43.

## 5 Conclusion

In this study, we developed an experimental setup to measure Raman spectroscopy and second harmonic generation simultaneously, and rapidly and quantitatively extract the second-order nonlinear optical tensor elements of a material. This technique takes advantage of the spatial and temporal mismatch of a Bessel-Gaussian beam at the laser focal point to

simultaneously measure SHG at normal and fixed incidence. Thanks to the development of a patented dichroic module that preserves the polarization state, the method was implemented on a confocal microscope and enables full polarization dependence measurements on microscopic samples, while minimizing movements of both the sample and optical components.

A numerical data analysis method, based on a ray-tracing model that accounts for each optical component of the instrument as well as the optical parameters of the sample, enables the full use of the light intensity distribution collected in the Fourier plane of the objective.

We fitted the SHG and Raman responses of LiNbO<sub>3</sub> together with the corresponding responses of KDP reference crystals and successfully extracted the nonlinear tensor elements. The values obtained are in close agreement with those reported in the literature.<sup>34,37-39</sup>

This new method offers a powerful and precise way to measure second- and possibly third-order nonlinear optical tensors in nano-objects. A key application is the rapid localization and characterization of 2D materials, which could greatly accelerate the fabrication of complex heterostructures. Inspired by X-ray diffraction or the structural biology Cryo-EM's approach,<sup>44</sup> the technique also enables global tensor fitting from polarization maps of randomly oriented dielectric nanoparticles.

## Acknowledgement

This project was supported by the Swiss National Science Foundation through projects CRSK-2-227400

## Supporting Information Available

See supplementary.pdf

## References

- (1) Aghigh, A.; Bancelin, S.; Rivard, M.; Pinsard, M.; Ibrahim, H.; Légaré, F. Second harmonic generation microscopy: a powerful tool for bio-imaging. *Biophysical Reviews* **15**, 43–70.
- (2) Multian, V.; Teyssier, J. Beam splitting/mixing module for an optical system and an associated optical system. 2024; US Patent App. 18/735,863.
- (3) Dai, Y.; He, C.; Wang, J.; Turcotte, R.; Fish, L.; Wincott, M.; Hu, Q.; Booth, M. Active compensation of extrinsic polarization errors using adaptive optics. *Optics Express* **27**, 35797.
- (4) Liu, Y.-C.; Lo, Y.-L.; Liao, C.-C. Compensation of non-ideal beam splitter polarization distortion effect in Michelson interferometer. *Optics Communications* **361**, 153–161.
- (5) Romijn, E. I.; Finnøy, A.; Kumar, R.; Lilledahl, M. B. Automated calibration and control for polarization-resolved second harmonic generation on commercial microscopes. *PLOS ONE* **13**, e0195027, Publisher: Public Library of Science.
- (6) Chou, C.-K.; Chen, W.-L.; Fwu, P. T.; Lin, S.-J.; Lee, H.-S.; Dong, C.-Y. Polarization ellipticity compensation in polarization second-harmonic generation microscopy without specimen rotation. *Journal of Biomedical Optics* **13**, 014005, Publisher: SPIE.
- (7) Ardizzone, I.; Teyssier, J.; Crassee, I.; Kuzmenko, A. B.; Mazzone, D. G.; Gawryluk, D. J.; Medarde, M.; van der Marel, D. Raman spectroscopic evidence for multiferroicity in rare earth nickelate single crystals. *Physical Review Research* **2021**, *3*, 033007, Publisher: American Physical Society.
- (8) app.speqqle. <https://www.speqqle.com>.
- (9) Cox, L. J. The Compensation of Instrumental Polarization by Inclined Mirrors. *Monthly Notices of the Royal Astronomical Society* **176**, 525–532.

(10) Bélanger, E.; Turcotte, R.; Daradich, A.; Sadetsky, G.; Gravel, P.; Bachand, K.; De Koninck, Y.; Côté, D. C. Maintaining polarization in polarimetric multiphoton microscopy. *Journal of Biophotonics* *8*, 884–888.

(11) Polarguard | polarisation maintaining dichroic optical module. <https://polarguard.ch>.

(12) Boyd, R. W. *Nonlinear optics*, 3rd ed.; Academic Press: Burlington, MA, 2008.

(13) Yamada, C.; Kimura, T. Anisotropy in second-harmonic generation from reconstructed surfaces of GaAs. *Physical Review Letters* *70*, 2344–2347, Publisher: American Physical Society.

(14) Heinz, T. F.; Loy, M. M. T.; Thompson, W. A. Study of Si(111) Surfaces by Optical Second-Harmonic Generation: Reconstruction and Surface Phase Transformation. *Physical Review Letters* *54*, 63–66, Publisher: American Physical Society.

(15) Tom, H. W. K.; Heinz, T. F.; Shen, Y. R. Second-Harmonic Reflection from Silicon Surfaces and Its Relation to Structural Symmetry. *Physical Review Letters* *51*, 1983–1986, Publisher: American Physical Society.

(16) Rendón-Barraza, C.; Timpu, F.; Grange, R.; Brasselet, S. Crystalline heterogeneity in single ferroelectric nanocrystals revealed by polarized nonlinear microscopy. *Scientific Reports* *9*, 1670, Number: 1 Publisher: Nature Publishing Group.

(17) Schmidt, C.; Riporto, J.; Uldry, A.; Rogov, A.; Mugnier, Y.; Dantec, R. L.; Wolf, J.-P.; Bonacina, L. Multi-Order Investigation of the Nonlinear Susceptibility Tensors of Individual Nanoparticles. *Scientific Reports* *6*, 25415, Number: 1 Publisher: Nature Publishing Group.

(18) Butet, J.; Bachelier, G.; Duboisset, J.; Bertorelle, F.; Russier-Antoine, I.; Jonin, C.; Benichou, E.; Brevet, P.-F. Three-dimensional mapping of single gold nanoparticles em-

bedded in a homogeneous transparent matrix using optical second-harmonic generation. *Optics Express* 18, 22314–22323, Publisher: Optica Publishing Group.

(19) Schwung, S. et al. Nonlinear optical and magnetic properties of BiFeO<sub>3</sub> harmonic nanoparticles. *Journal of Applied Physics* 116, 114306.

(20) Lien, C.-H.; Tilbury, K.; Chen, S.-J.; Campagnola, P. J. Precise, motion-free polarization control in Second Harmonic Generation microscopy using a liquid crystal modulator in the infinity space. *Biomedical Optics Express* 4, 1991–2002, Publisher: Optica Publishing Group.

(21) Chen, C.; Chen, X.; Gu, H.; Jiang, H.; Zhang, C.; Liu, S. Calibration of polarization effect of a high-numerical-aperture objective lens with Mueller matrix polarimetry. *Measurement Science and Technology* 30, 025201.

(22) Chen, Z.; Hua, L.; Pu, J. In *Progress in Optics*; Wolf, E., Ed.; Progress in Optics; Elsevier, Vol. 57; pp 219–260.

(23) Shatrovoy, O. Second-harmonic generation with Bessel beams. M.Sc. thesis, Boston University, 2016.

(24) Salter, P. S.; Booth, M. J. Adaptive optics in laser processing. *Light: Science & Applications* 8, 110, Number: 1 Publisher: Nature Publishing Group.

(25) Torchinsky, D. H.; Chu, H.; Qi, T.; Cao, G.; Hsieh, D. A low temperature nonlinear optical rotational anisotropy spectrometer for the determination of crystallographic and electronic symmetries. *Review of Scientific Instruments* 85, 083102.

(26) Lu, B.; Tran, J. D.; Torchinsky, D. H. Fast reflective optic-based rotational anisotropy nonlinear harmonic generation spectrometer. *Review of Scientific Instruments* 90, 053102.

(27) Harter, J. W.; Niu, L.; Woss, A. J.; Hsieh, D. High-speed measurement of rotational anisotropy nonlinear optical harmonic generation using position-sensitive detection. *Optics Letters* **40**, 4671.

(28) Netz, R.; Feurer, T.; Wolleschensky, R.; Sauerbrey, R. Measurement of the pulse-front distortion in high-numerical-aperture optics. *Applied Physics B* **2000**, *70*, 833–837.

(29) Caron, C. F. R.; Potvliege, R. M. Phase matching and harmonic generation in Bessel–Gauss beams. *JOSA B* **1998**, *15*, 1096–1106, Publisher: Optica Publishing Group.

(30) Rao, A. S. A conceptual review on Bessel beams. *Physica Scripta* **2024**, *99*, 062007, Publisher: IOP Publishing.

(31) Arlt, J.; Dholakia, K.; Allen, L.; Padgett, M. J. Efficiency of second-harmonic generation with Bessel beams. *Physical Review A* **1999**, *60*, 2438–2441.

(32) Thibon, L.; Lorenzo, L. E.; Piché, M.; De Koninck, Y. Resolution enhancement in confocal microscopy using Bessel-Gauss beams. *Optics Express* **2017**, *25*, 2162–2177.

(33) McGloin, D.; Dholakia, K. Bessel beams: Diffraction in a new light. *Contemporary Physics* **2005**, *46*, 15–28.

(34) Eimerl, D. Electro-optic, linear, and nonlinear optical properties of KDP and its iso-morphs. *Ferroelectrics* **1987**, *72*, 95–139.

(35) Kolybayeva, M. I.; Pritula, I. M.; Puzikov, V. M.; Salo, V. I.; Garnov, S. V.; Klimentov, S. M. Increase of the laser damage threshold of KDP single crystals by their heat treatment. Boulder, CO, 1995; pp 84–87.

(36) Nikogosian, D. N.; Nikogosyan, D. N. *Nonlinear optical crystals: a complete survey*; Springer-Science: New York, 2005.

(37) Shoji, I.; Kondo, T.; Kitamoto, A.; Shirane, M.; Ito, R. Absolute scale of second-order nonlinear-optical coefficients. *Journal of the Optical Society of America B* **1997**, *14*, 2268.

(38) Roberts, D. Simplified characterization of uniaxial and biaxial nonlinear optical crystals: a plea for standardization of nomenclature and conventions. *IEEE Journal of Quantum Electronics* **1992**, *28*, 2057–2074.

(39) Boyd, G. D.; Miller, R. C.; Nassau, K.; Bond, W. L.; Savage, A. LiNbO<sub>3</sub>: An efficient phase matchable nonlinear optical material. *Applied Physics Letters* **1964**, *5*, 234–236.

(40) Huang, H.; Kosc, T. Z.; Kessler, T. J.; Demos, S. G. Modeling of transverse stimulated Raman scattering in KDP/DKDP in large-aperture plates suitable for polarization control. *High Power Laser Science and Engineering* **2023**, *11*, 05000e54.

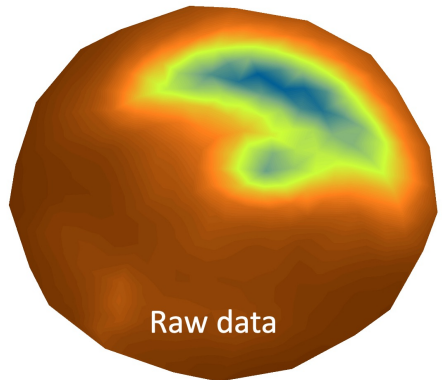
(41) Demos, S. G.; Raman, R. N.; Yang, S. T.; Negres, R. A.; Schaffers, K. I.; Henehan, M. A. Measurement of the Raman scattering cross section of the breathing mode in KDP and DKDP crystals. *Optics Express* **2011**, *19*, 21050–21059, Publisher: Optica Publishing Group.

(42) Bagheri, M.; Komsa, H.-P. High-throughput computation of Raman spectra from first principles. *Scientific Data* **2023**, *10*, 80, Publisher: Nature Publishing Group.

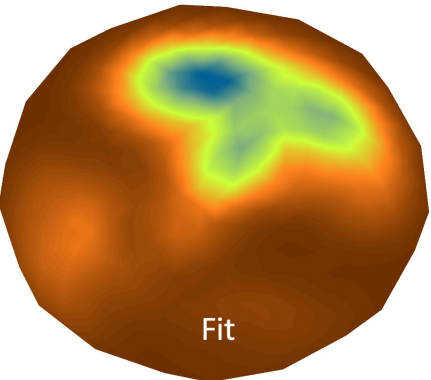
(43) Galinetto, P.; Marinone, M.; Grando, D.; Samoggia, G.; Caccavale, F.; Morbiato, A.; Musolino, M. Micro-Raman analysis on LiNbO<sub>3</sub> substrates and surfaces: Compositional homogeneity and effects of etching and polishing processes on structural properties. *Optics and Lasers in Engineering* **2007**, *45*, 380–384.

(44) Dubochet, J.; Adrian, M.; Chang, J. J.; Homo, J. C.; Lepault, J.; McDowall, A. W.; Schultz, P. Cryo-electron microscopy of vitrified specimens. *Nature* **1988**, *308*, 32–36.

a Fourier plane image

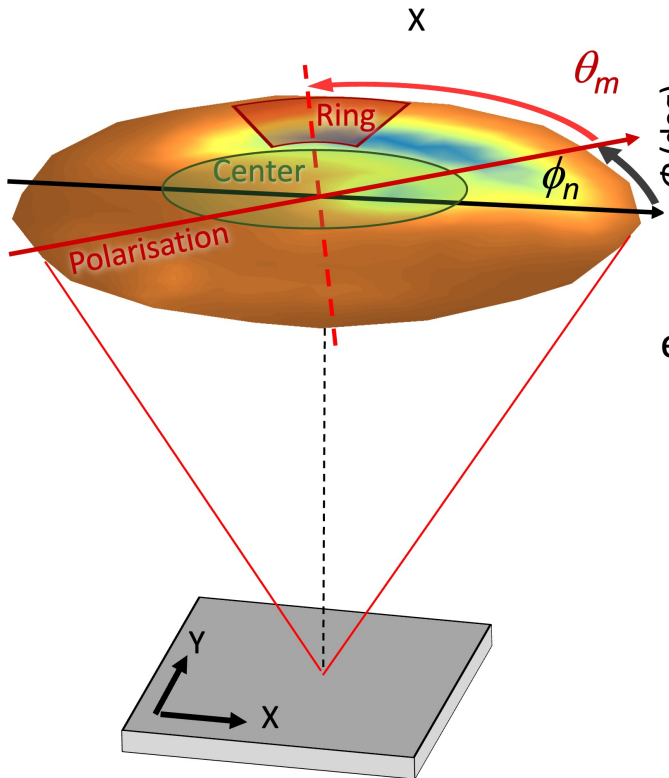


b Fit using ray tracing model

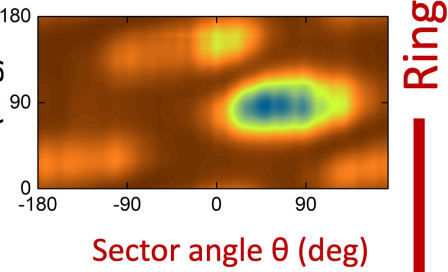


LiNbO<sub>3</sub> ab  $\phi_n = 69^\circ$  parallel

c



$\int \text{sector}(\phi_n, \theta_m)$



$\int \text{center}(\phi_n)$

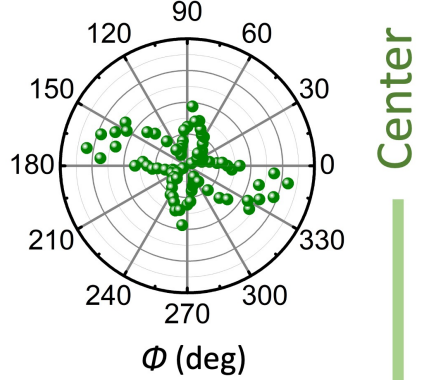


Figure 3: a) SHG image collected at Fourier plane on LiNbO<sub>3</sub> for an incoming polarisation  $\phi_n = 69^\circ$  in parallel mode. b) fit of the Fourier image. c-d) Procedure to display the set of raw and fitted Fourier maps into a single  $\phi$  /  $\theta$  polar map . c) Scheme of the analyzed ring identifying angle  $\phi_n$  as the angle of the incoming polarization relative to  $x$  axis and  $\theta_m$  the angle between the incoming polarization and the  $m^{\text{th}}$  sector. d) resulting polar map after integration of all sectors relative to the two angles. e) Integrated values of the central intensity as a function of  $\phi$ .

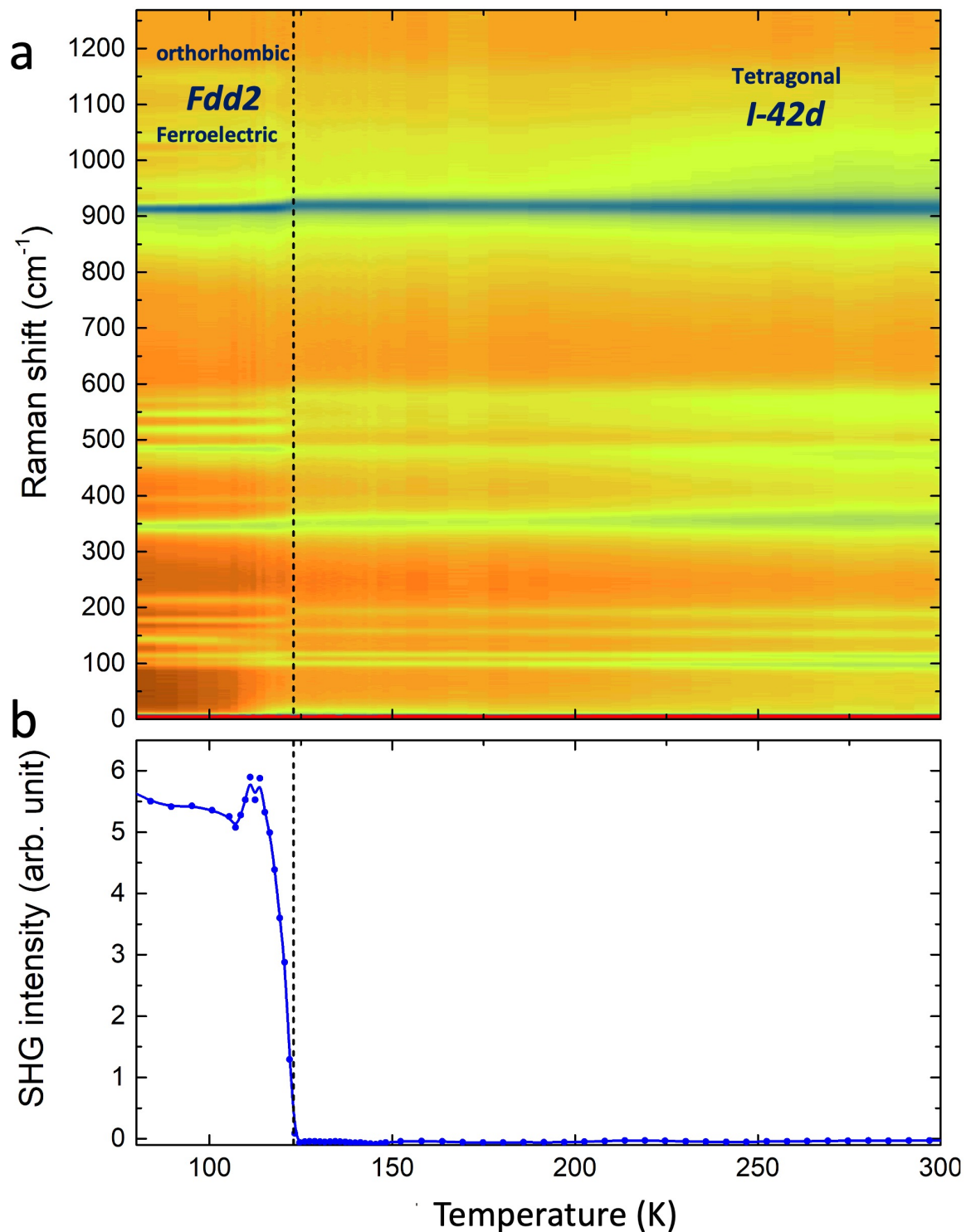


Figure 4: a) Raman and b) global SHG temperature dependence of a KDP crystal. dashed line corresponds to the temperature of the structural transition.

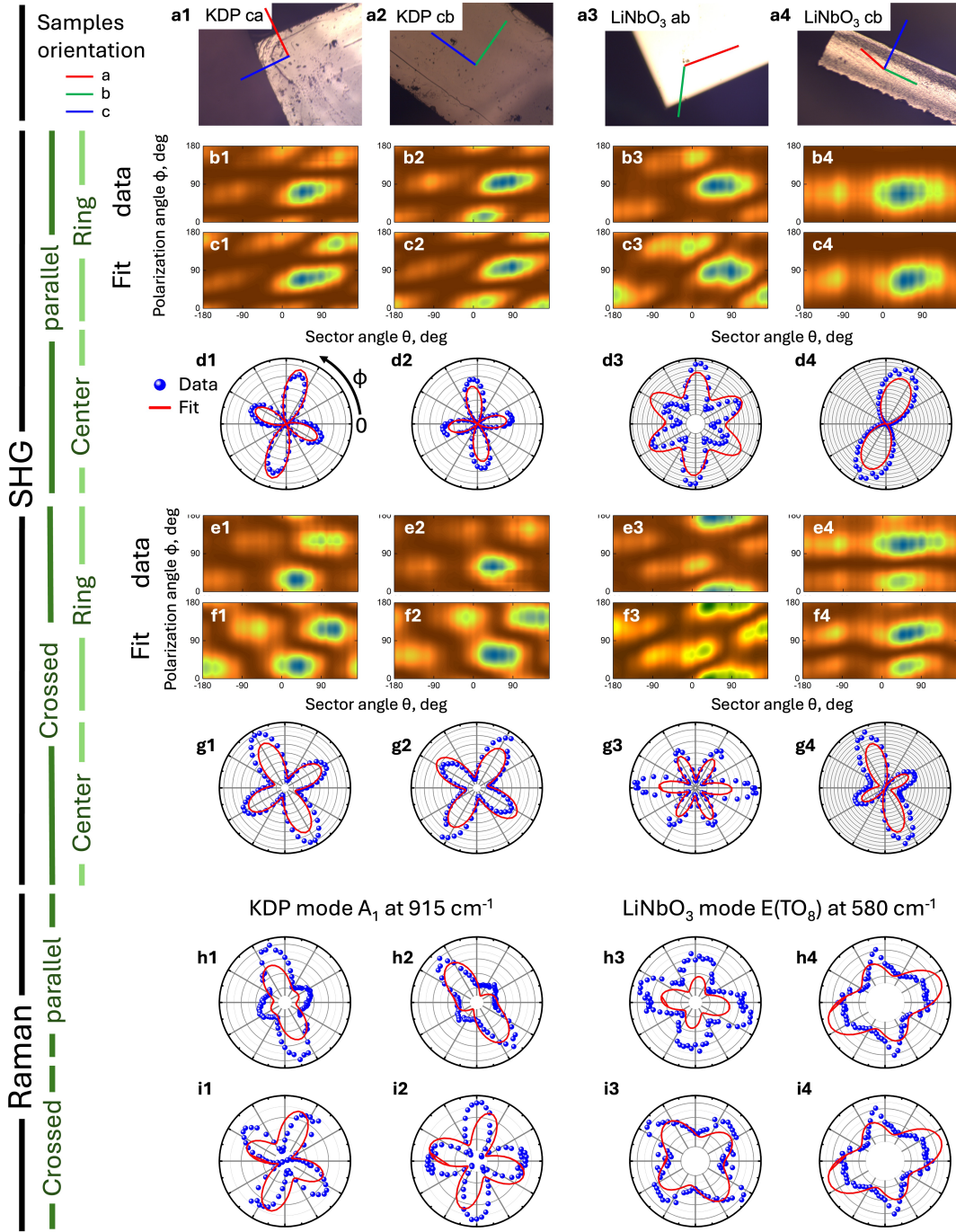


Figure 5: Full set of polarization resolved SHG (b-g) and Raman (h,i) data with the corresponding fit using the unified model described in the text. Each column corresponds to KDP (1,2) or LiNbO<sub>3</sub> (3,4) crystals with specific orientation. **a**) Optical images of the crystals with crystallographic axis (a red, b green, c blue). **b** and **e**, experimental SHG intensity maps in parallel and crossed configurations respectively extracted from the "ring" part of images in Fourier plane. **c** and **f**, corresponding fits. **d** and **g**, polarization resolved SHG intensities in parallel and crossed configurations respectively, extracted from the "central" part of the images in Fourier plane. **h** and **i**, polarization resolved Raman scattering intensities measured in parallel and crossed configurations respectively. (h,i;1,2), A<sub>1</sub> Raman mode of KDP at 915 cm<sup>-1</sup> and (h,i;3,4), E Raman mode of LiNbO<sub>3</sub> at 580 cm<sup>-1</sup> for corresponding orientation of the crystals. Legends and axes of all polar plots match those in d1.